Supplemental material
Stability of ablation flows in inertial confinement fusion: non-modal effects

G. Varillon,[1,2] J.-M. Clarisse,[1] and A. Couairon[2]

[1] *CEA, DAM, DIF, F-91297 Arpajon, France*

[2] *CPHT, CNRS, Ecole Polytechnique, Institut Polytechnique de Paris, Route de Saclay, 91128 Palaiseau, France*[*]

(Dated: November 2, 2020)

I. BASE FLOWS

For the choice $\gamma = 5/3$, $(\mu, \nu) = (2, 13/2)$, Eq. (1) describes the motion of a monatomic gas with the radiative conduction model of Kramers [1]. This modeling is an approximation for the ablation of a fusion capsule ablator by hohlraum x rays in current ICF laser facilities. This approximation is relevant to the ablator opaque portion which stays at temperatures below a few 10^6 Kelvin degrees and at thermodynamic equilibrium. Radiation diffusive effects then dominate those of thermal conduction and viscosity, and radiation pressure and energy are negligible in front of their material counterparts. If Eq. (1) cannot render non-gray irradiation effects, it contains the basic diffusion mechanism at stake, at the hydrodynamic scale, in this ablation process. Such a modeling of radiative ablation compares favorably with any of the models previously used for investigating hydrodynamic stability of ablation flows and designing experiments (e.g. see Ref. 2 and references therein): it retains the same compressible inviscid fluid model for a polytropic gas with a nonlinear heat conductivity in powers of the density and temperature. However, none of the additional restrictive assumptions (e.g. flow steadiness, constant and uniform acceleration field, quasi-isobaric approximation, semi-infinite fluid domains) that are commonly used in these other stability studies of ablation flows, are invoked here.

A. Self-similar ablation waves

Self-similar reductions of Eq. (1) occur when considering a semi-infinite slab ($m \geq 0$), initially such that (ρ, v_x, T) = (const, 0, 0), is subject to boundary conditions, at the material surface $m = 0$, of the form

$$\varphi_x(0,t) = \mathcal{B}_\phi t^{3\alpha-3}, \quad p(0,t) = \mathcal{B}_p t^{2\alpha-2}, \quad \text{for } t \geq 0, \tag{5}$$

with $\alpha = (2\nu-1)/(2\nu-2)$: cf. Refs. [3–5]. Self-similar solutions to Eq. (1) with such initial and boundary conditions are computed by means of an adaptive multidomain Chebyshev method capable of a high accuracy description of the flow down to its finest scales [6]. For the present study, the base-flow solution $(\mathcal{B}_\phi, \mathcal{B}_p) = (0.8, 0.31)$ that has been retained (Fig. 1), is computed using 39 domains with 50 collocation points each. This numerical method has been verified against results from a hydrocode simulation [4, Fig. 11] of an IBVP defined after Eqs. (1) and (5), and approximate analytical solutions [5, App. A].

The solution $(\mathcal{B}_\phi, \mathcal{B}_p) = (0.8, 0.31)$ has been chosen among a large set of self-similar ablation waves [5], on the basis of its hydrodynamic characteristic numbers which are typical of the early stage of a capsule implosion: subsonic ablation Mach number, high Froude number (> 80) at the ablation front, steep ablation front, and fast expansion flow with Chapman–Jouguet point (Fig. 1). During this so-called *shock transit stage*, the leading shock front of the ablation wave has not yet reached the ablator inner surface. In actual or simulated implosions, neither the radiative heat flux at the capsule external surface, nor the pressure exerted by the hohlraum filling gas, nor the capsule ablator opacity comply with the constraints required for self-similarity. Yet, spatial profiles of self-similar flow variables possess essential features that resemble those obtained in simulations of the shock transit stage of a realistic ICF capsule design: cf. Ref. 5, Fig. 2. In that respect, results obtained with the chosen self-similar ablation wave may be equally used in connection with a capsule ablation simulation.

[*] gregoire.varillon@polytechnique.edu

B. Connection with a capsule implosion simulation

Considering a particular ICF capsule design (here that given in Ref. 7, Fig. 1) and its implosion simulation with an ICF hydrocode (code FCI2, cf. Ref. 8), time and length scales may be defined respectively from the duration of the ablation flow regime within the period of the shock transit stage, and the distance travelled by the leading shock front during this period. The starting time of this ablation regime is established as being one of the earliest times for which, in the simulation, an ablation wave structure with a non-vanishing extent of its shock-compressed region is clearly identified within the ablator, presently $\bar{t}_0 = 2.8\,\mathrm{ns}$. This starting time is associated to the reference time of the self-similar ablation wave which may be set arbitrarily to be $t_0 = 1$. The final time of the ablation regime, in the simulation, is taken to be the time of the leading shock-front breakout at the ablator inner surface, here $\bar{t}_1 = 12.9\,\mathrm{ns}$. Over the flow period thus defined, a linear perturbation initiated at the ablation front may propagate as a forward acoustic wave towards the shock front then back to the ablation front as an advected entropy wave [9], the whole being repeated a limited number of times. This finite sequence of propagation-then-advection of perturbations between the ablation and shock fronts is a key mechanism of perturbation dynamics during the shock transit stage: e.g. see Refs. [10, 11]. Seeking to reproduce the same wave sequence in the present self-similar flow is therefore desirable, and presently sets a lower bound on the maximum time horizon for this flow, here $t_1 = 8$. The correspondence of flow durations and shock travelled distances between the simulated flow and the self-similar solution defines then time and length scales for the latter, in effect $t_\star = 1.44\,\mathrm{ns}$ and $l_\star = 19.04\,\mu\mathrm{m}$.

II. LINEAR PERTURBATIONS

The system of equations for the yz-Fourier components of the linear perturbations for the density, $\widehat{\rho}$, longitudinal velocity, $\widehat{v}_x$, transverse divergence of the transverse velocity, $\widehat{d}_\perp$, and temperature, $\widehat{T}$, reads (cf. Ref. 12 and Eq. 4 in Ref. 9)

$$\begin{aligned}
&\partial_t\widehat{\rho} + \rho^2\,\partial_m\widehat{v}_x + \rho\,\partial_m v_x\,\widehat{\rho} + \rho\,\partial_m\rho\,\widehat{v}_x + \rho\,\widehat{d}_\perp = 0,\\
&\partial_t\widehat{v}_x + T\,\partial_m\widehat{\rho} + \rho\,\partial_m\widehat{T} - \rho^{-1}\,T\,\partial_m\rho\,\widehat{\rho} + \rho\,\partial_m v_x\,\widehat{v}_x + \partial_m\rho\,\widehat{T} = 0,\\
&\partial_t\widehat{d}_\perp - k_\perp^2\,\rho^{-1}\,T\,\widehat{\rho} - k_\perp^2\,\widehat{T} = 0,\\
&\partial_t\widehat{T} + \mathrm{C}_v^{-1}\,\rho\,\psi_{T'}\,\partial^2_{m^2}\widehat{T} + \mathrm{C}_v^{-1}\,\psi_\rho\,\partial_m\widehat{\rho} + \mathrm{C}_v^{-1}\,p\,\partial_m\widehat{v}_x + \mathrm{C}_v^{-1}\big[\partial_m(\rho\,\psi_{T'}) + \psi_T\big]\,\partial_m\widehat{T}\\
&\quad + \mathrm{C}_v^{-1}\big[\partial_m\psi_\rho - \rho^{-1}\,\partial_m\psi\big]\,\widehat{\rho} + \rho\,\partial_m T\,\widehat{v}_x + \mathrm{C}_v^{-1}\,T\,\widehat{d}_\perp + \mathrm{C}_v^{-1}\big[\rho\,\partial_m v_x + \partial_m\psi_T - k_\perp^2\,\rho^{-1}\,\psi_{T'}\big]\,\widehat{T} = 0,
\end{aligned} \tag{6}$$

with the convention

$$\psi(\rho, T, \partial_x T) \equiv -\rho^{-\mu}T^\nu\,\partial_x T = -\rho^{-\mu}T^\nu\rho\,\partial_m T,$$

and the notations ψ_ρ, ψ_T, $\psi_{T'}$ for the partial derivatives of the heat-flux function ψ with respect to the density, the temperature, and the temperature gradient. When considering self-similar ablation waves solutions to Eqs. (1) and (5), boundary conditions for linear perturbations at the location, $m = m_{\mathrm{sf}}(t)$, of the leading shock-wave front are derived from the non-isothermal Rankine–Hugoniot relations for a perturbed shock front [12, App. B]. At the fluid external boundary, $m = 0$, perturbation boundary conditions correspond to the continuity of the pressure and heat flux supplemented by the kinematic boundary condition at this material surface (Eq. 5 of Ref. 9). For the present study, zero perturbations for the state upstream to the shock front and for the incident heat flux and boundary pressure at the fluid external surface are retained.

Solutions to IBVPs based on Eq. (6) are computed, in space, using the same multidomain Chebyshev method as for Eq. (1) and, in time, with a three-step implicit-explicit Runge–Kutta scheme. Verification of this computational method has been performed in several instances by comparisons with exact perturbation solutions [13–16]. This method has also been previously used for computing linear perturbation responses in perturbed configurations of ablation waves relevant to ICF and corresponding to illumination asymmetries [3, 12, 17, 18] and to the ablative Richtmyer–Meshkov instability [18]. Corresponding results were analyzed to be in general agreement with previous models of perturbation evolution for laser imprinting [10, 19] and ablative Richtmyer–Meshkov instability [11, 20] with, however, distinctive differences emphasizing, in particular, the influence of the base-flow unsteadiness and stretching: see [3, 12, 18] for details and discussions.

III. BASIC NOTIONS OF NON-MODAL ANALYSIS

Modal stability analysis infers the stability of a dynamical system, ruled by an equation like Eq. (2), from the sole basis of the least stable eigenvalue of its evolution operator, $\mathcal{A}$. This analysis is correct if the eigenmodes of $\mathcal{A}$

form an orthogonal set—equivalently, if the operator $\mathcal{A}$ is normal—and is otherwise only indicative of the long-time behavior of the system. For finite-time horizons, a non-normal operator $\mathcal{A}$ may induce transient growth of the system state variable through eigenmode interactions, even if the system is stable according to modal analysis [21, 22]. For a time-dependent evolution operator as in Eq. (2), the growth of the state variable $\widehat{\mathbf{U}}$ can be assessed at any given time t_* from the instantaneous growth rate of some chosen norm of $\widehat{\mathbf{U}}$, namely [23]

$$\sigma(t_*) \equiv \left(\frac{1}{\|\widehat{\mathbf{U}}\|^2} \frac{\mathrm{d}\|\widehat{\mathbf{U}}\|^2}{\mathrm{d}t} \right)\Big|_{t_*} = 2\,\mathrm{Re}\left(\frac{\langle \widehat{\mathbf{U}}, \mathcal{A}\,\widehat{\mathbf{U}} \rangle}{\langle \widehat{\mathbf{U}}, \widehat{\mathbf{U}} \rangle} \right)\Big|_{t_*}, \tag{7}$$

where $\langle \cdot, \cdot \rangle$ denotes the scalar product associated to this norm and $\|\widehat{\mathbf{U}}\|^2 = \langle \widehat{\mathbf{U}}, \widehat{\mathbf{U}} \rangle$. The ratio

$$\frac{\langle \widehat{\mathbf{U}}, \mathcal{A}\,\widehat{\mathbf{U}} \rangle}{\langle \widehat{\mathbf{U}}, \widehat{\mathbf{U}} \rangle}\Big|_{t_*},$$

is known as the *numerical range* of the operator $\mathcal{A}|_{t_*}$ and defines a region of the complex plane which, in the case of an operator $\mathcal{A}$ of finite dimension, contains the spectrum of $\mathcal{A}|_{t_*}$. For a non-normal operator, as it is generally the case, the numerical range is larger than the convex hull of the spectrum. In the case of a normal operator, the two regions coincide [24]. In particular, this numerical range may protrude into the unstable half-plane ($\mathrm{Re} > 0$) even though the spectrum of $\mathcal{A}|_{t_*}$ may be confined to the stable half-plane ($\mathrm{Re} < 0$): cf. Fig. 5(c). In such a case *non-modal growth* occurs, i.e. an initial amplification—*transient growth*—of $\widehat{\mathbf{U}}$ may be observed, although all eigenvalues are stable according to modal stability analysis. The potential for such a transient growth is measured by means of the maximum of the instantaneous growth rate $\sigma(t_*)$ over all non-zero possible states, or *numerical abscissa* of $\mathcal{A}|_{t_*}$, say

$$\sigma_* \equiv \max_{\widehat{\mathbf{U}}} \sigma(t_*). \tag{8}$$

This numerical abscissa is given by the largest eigenvalue of the normal operator $(\mathcal{A} + \mathcal{A}^\dagger)|_{t_*}$ and is achieved when $\widehat{\mathbf{U}}$ is the principal eigenmode of this operator (cf. Ref. 23), thus defining the *optimal-growth initial condition* at time t_*, say $\widehat{\mathbf{U}}_*^{\mathrm{opt}}$. The situation of non-normal growth described above corresponds to the case $\max \mathrm{Re}(\Lambda) < 0 < \sigma_*$, where Λ denotes the eigenvalues of $\mathcal{A}_{t_*}$. However non-modal effects are not restricted to this specific configuration. Indeed, when $0 < \max \mathrm{Re}(\Lambda) < \sigma_*$ [Fig. 5(b)], the system is unstable at all time horizons but may display a transient growth that is faster than the exponential growth of the least stable eigenmode. For $\max \mathrm{Re}(\Lambda) < \sigma_* \leq 0$ [Fig. 5(a)], the system is stable, here again at all time horizons, but with an eventual transient decay that is slower than the exponential decay of the least stable eigenmode.

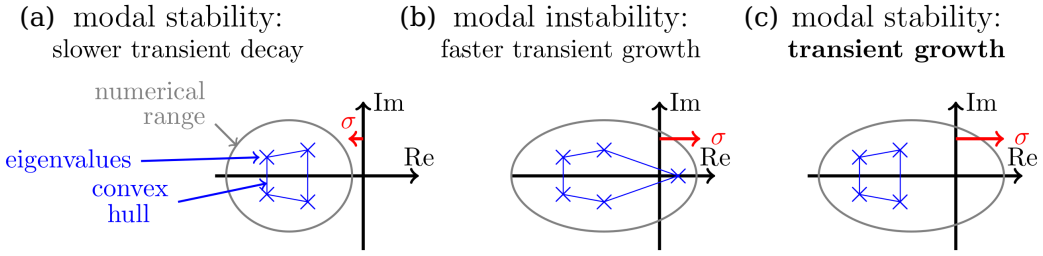

FIG. 5: Schematic layouts in the complex plane of eigenvalues and numerical ranges corresponding to: (a) modal stability with slower non-modal transient decay, (b) modal instability with faster non-modal transient growth, and (c) modal stability with non-modal transient growth.

IV. TRANSIENT GROWTH MECHANISM: CONSTRUCTIVE INTERACTION OF COMPRESSIBLE WAVES

A. Non-modal stability results

The non-modal stability analysis presently conducted on a self-similar ablation wave focuses on flow perturbations that, at some flow location x_* and at the chosen time $t_* = t_0$, yield the maximum values, σ_0, of the instantaneous

growth rate (7), i.e. that are the fastest growing modes at this time and location. Within the restriction that the flow is locally weakly stratified over the longitudinal length scales of the perturbations (i.e. $\varkappa_x(x_*) \gg 1$), this analysis has identified flow regions and perturbation characteristic scales, $\varkappa_x$ and $\varkappa_\perp$, where non-modal growth [configuration of Fig. 5(c)] and modal growth [configuration of Fig. 5(b)] are expected to occur initially: cf., respectively, the coloured and black areas in Fig. 2. For both cases it turns out that the maximum instantaneous growth rate σ_0 is dominated by a non-modal growth, in other words the fastest perturbation growth at t_0 is much faster than the growth of the least stable eigenmode of the flow: $\sigma_0 > 0$ with $\sigma_0 \gg \max \mathrm{Re}(\Lambda)$, even when $\max \mathrm{Re}(\Lambda) > 0$. As apparent in Fig. 2, this dominance increases as the perturbation longitudinal wavelength decreases. Non-modal growth is also found to be enhanced at shorter transverse wavelengths, both in terms of values of σ_0 (Table I) and ranges of the perturbation longitudinal length scale. These observations depict a situation where, for all the perturbation wavelengths that have been tested, the local short-term dynamics of flow fluctuations are determined by non-modal effects, implying that modal stability analysis is nowhere suitable for their predictions.

B. Mechanism of transient growth

The dynamics of perturbations in the flow compression region, i.e. between the shock front and the ablation layer, during the shock transit stage of a capsule implosion deserve special attention. These dynamics are especially important for the outcome of the implosion since they set the initial conditions for the subsequent acceleration stage during which major perturbation amplification occurs due to the ablative Rayleigh–Taylor instability. The computations of perturbation evolutions, started from the optimal-growth initial conditions of Eq. (4) at locations within the compression region, show that the fastest transient growth comes from the constructive interaction between the different fundamental waves—or Kovásznay modes [25]—that constitute these initial perturbations (see Fig. 4 for $t \simeq 1$). For the sample of transverse wavelengths considered (Table 1), these fundamental waves are dominantly of the acoustic and entropy types, the initial vorticity waves being of negligible contributions. This mechanism of wave interaction is intrinsic to compressible fluid motion and is expected to occur in the compression regions of actual ablation flows since in such regions effects of advection prevail over those of heat transfer.

These results when used in connection with a simulated capsule implosion (see Sec. I B), furnish data [Table 1(b)] that fall within the characteristic sizes of known bulk inhomogeneities of currently used ablator materials [26]. In the flow compression region during the shock transit stage, these materials are in a complex liquid state (densities of several $\mathrm{g\,cm^{-3}}$, temperatures around 1 eV), partially dissociated and ionized, which is far from being known with sufficient details and is still the object of ongoing studies. The characteristic growth times $\sigma_{\mathrm{AT}}^{-1}$ of the identified transient growths are especially small: tenths of a picosecond [Table 1(b)]. For CH plastic ablators, such times are an order of magnitude larger than the acoustic transit time between atoms and thus compatible with the assumption of local thermodynamic equilibrium for translation motions. Non-equilibrium effects associated to rotation and vibration motions cannot be ruled out but their assessment would require a more detailed knowledge of these ablator materials under these liquid state conditions. Effects of thermal conduction and of viscosity on this transient growth mechanism would also need to be assessed at the perturbation scales of tens of nanometers which are involved [Table 1(b)]. But here again adequate data and modelings relevant to these specific liquid states are currently unsufficient for doing so.

Past the initial growth, the contructive interaction of acoustic and entropy waves associated to the present transient growth leads to perturbation amplifications in the range 5–20 in a few picoseconds (Fig. 3). These amplifications, as the instantaneous growth rates, are enhanced by a reduction of the transverse wavelength: compare the perturbation norm responses, $\|\widehat{\mathbf{U}}\|/\|\widehat{\mathbf{U}}\|_{|t_0}$, for the two wavenumbers $\varkappa_\perp = 1.40$ ($\lambda_\perp \approx 100\,\mu$m) and $\varkappa_\perp = 131.5$ ($\lambda_\perp \approx 1\,\mu$m) in Fig. 3. The residual amplifications, once the initial wave interactions have ended [i.e. after event A in Figs. 3 and 4(a)], slowly decrease over tenths of nanoseconds while remaining at significant levels. Such evolutions correspond to the advection, or propagation, (see Fig. 4) of the three kinds of waves (i.e. entropy waves plus forward and backward propagating acoustic waves) that are present in the initial perturbations, and to their subsequent interactions with either the ablation layer (event B) or the shock front (event D). All of these processes and trends are reproduced for other locations of the optimal-growth initial conditions Eq. 4, with a systematic enhancement of amplifications when the zone of transient growth, or *transient-growth spot*, is close and upstream to the ablation layer, as illustrated in Fig. 6 by comparison with Fig. 3. This increased influence of a transient-growth spot located close to the ablation layer is also obvious from the dynamics of the ablation front deformations (Fig. 7).

This analysis of the consequences of constructive interactions of compressible waves on the compression region and ablation layer of an ablation flow presently involves isolated transient-growth spots that are of limited spatial extents (in effect, five longitudinal wavelengths). The conditions for the occurrence of such constructive interactions—the presence of acoustic and entropy plane waves of identical, or proportional, longitudinal wavelengths—are likely to be met in ablators presenting bulk material inhomogeneities. In such configurations, the leading shock front of the ablation wave, encountering these inhomogeneities, emits backward propagating acoustic waves and leaves

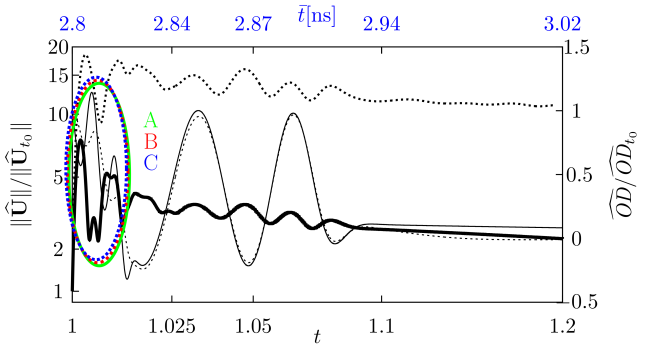

FIG. 6: Amplification of the perturbation norm, $\|\widehat{\mathbf{U}}\|/\|\widehat{\mathbf{U}}\|_{t_0}$, (thick lines—left axis) and of the optical depth perturbation, $\widehat{\mathrm{OD}}/\widehat{\mathrm{OD}}|_{t_0}$ (thin lines—right axis), for initial conditions Eq. 4 at a flow location immediately upstream to the ablation layer at $t = 1$, $x_* = -0.11$, with $\varkappa_x = 1758.$, $\varkappa_\perp = 1.40$ (solid) or $\varkappa_\perp = 131.5$ (dash). Remarkable events in the evolution of $\|\widehat{\mathbf{U}}\|$ equivalent to those of Figs. 3 and 4 are identified by letters A to C.

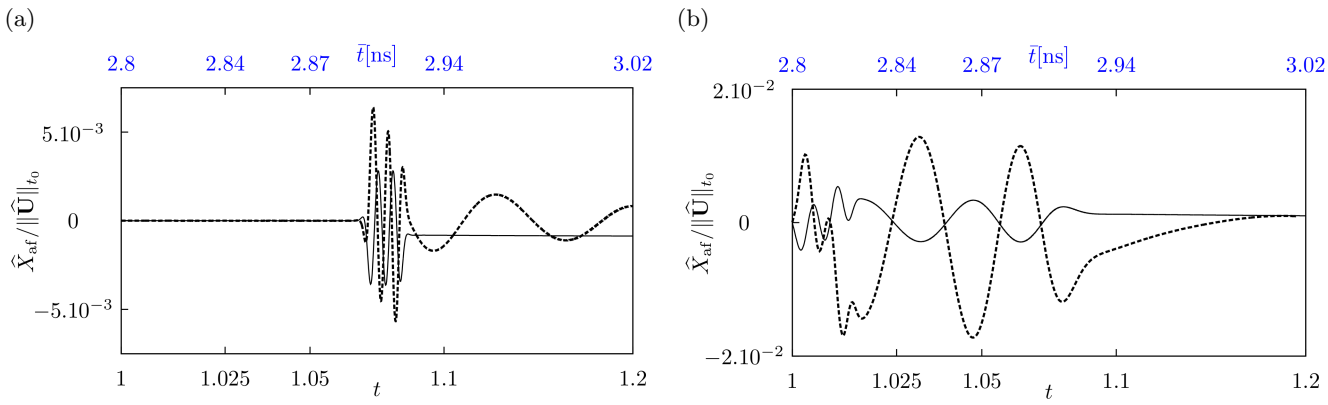

FIG. 7: Time evolutions of the ablation front deformation, normalized by $\|\widehat{\mathbf{U}}\|_{t_0}$, for initial conditions Eq. 4 at (a) a midpoint location within the compression region, $x_* = -0.06$, and (b) a location immediately upstream to the ablation layer, $x_* = -0.11$, with $\varkappa_x = 1758.$, $\varkappa_\perp = 1.40$ (solid) or $\varkappa_\perp = 131.5$ (dash).

entropy/vorticity waves in the flow compression region downstream (cf. Ref. [27]). These waves will trigger emission, from the ablation layer, of forward propagating acoustic waves—as in the case of event B in Fig. 4(a)—which will in turn interact with upstream acoustic and entropy waves, at times constructively. For randomly distributed material inhomogeneities, constructive interactions will occur repeatedly giving birth to distributions of transient-growth spots within the compressed portion of the ablator. The repetitive encounters of these spots with the ablation layer could result in an enhanced level of perturbations, including ablative Rayleigh–Taylor modes, at the onset of the acceleration phase of a capsule implosion. Besides, this process could foster a build up of perturbations over a wide range of characteristic lengths and over times shorter than the duration of the shock transit phase, leading possibly to local transitions to nonlinear regimes. Assessing the possibility of such mechanisms and their consequences for an ICF capsule ablation would require flow simulations not only at extremely fine spatial resolutions, which so far have been undertaken only once [28], but also, given the nature of the transient-growth mechanism, capable of a high fidelity rendering of acoustic phenomena at very disparate scales—something for which ICF hydrodynamics codes are not particularly suited.

Experimental detection of the above described mechanisms is yet another challenge. HDC materials for ablators can hardly be processed so as to impose controlled bulk inhomogeneities, similarly to what has been done for surface roughness or oxygen concentration in CH plastic ablators. Therefore the detection of transient growth events mainly relies on improvement of diagnostics. Firstly, current diagnostics do not have sufficient temporal resolutions to capture sub-nanosecond growth phenomena. Secondly, optical depth measurements in the longitudinal direction are blind to compressible perturbation modes, as shown on Figs. 3 and 6. Optical depth measurements in a direction transverse to the flow could yield some information about the dynamics and spatial structures of perturbations in the flow compression region, but under conditions of sufficiently high temporal and spatial resolutions that so far are not

available.

[1] Y. B. Zel'dovich and Y. P. Raizer, *Physics of shock waves and high-temperature hydrodynamic phenomena* (Academic Press, New York, 1967).
[2] V. Bychkov et al., Prog. Energy Combust. Sci. **47**, 32 (2015).
[3] F. Abéguilé et al., Phys. Rev. Lett. **97**, 035002 (2006).
[4] C. Boudesocque-Dubois et al., J. Fluid Mech. **603**, 151 (2008).
[5] J.-M. Clarisse et al., J. Fluid Mech. **848**, 219 (2018).
[6] C. Boudesocque-Dubois et al., J. Comput. Phys. **235**, 723 (2013).
[7] Y. Saillard, C. R. Acad. Sci. Paris, Series IV **1**, 705 (2000).
[8] E. Buresi et al., Laser Part. Beams **4**, 531 (1986).
[9] G. Varillon et al., Phys. Rev. E **101**, 043215 (2020).
[10] V. N. Goncharov et al., Phys. Plasmas **7**, 2062 (2000).
[11] Y. Aglitskiy et al., Phil. Trans. R. Soc. A **368**, 1739 (2010).
[12] J.-M. Clarisse et al., J. Fluid Mech. **609**, 1 (2008).
[13] C. Boudesocque-Dubois et al., J. Comput. Phys. **184**, 592 (2003).
[14] F. Abéguilé, Thèse de doctorat, Université de Paris 6 (2004).
[15] S. Gauthier et al., Int. J. Pure Appl. Math. **24**, 553 (2005).
[16] G. Varillon, Thèse de doctorat, Université Paris-Saclay, École polytechnique (2019).
[17] V. Lombard et al., Europhys. Lett. **84**, 25001 (2008).
[18] J.-M. Clarisse et al., Phys. Scr. **91**, 074005 (2016).
[19] V. N. Goncharov et al., Phys. Plasmas **13**, 012702 (2006).
[20] V. N. Goncharov, Phys. Rev. Lett. **82**, 2091 (1999).
[21] L. N. Trefethen et al., Science **261**, 578 (1993).
[22] P. J. Schmid, Annu. Rev. Fluid Mech. **39**, 129 (2007).
[23] P. J. Schmid and D. S. Henningson, *Stability and transition in shear flows* (Springer, New-York, 2001).
[24] R. A. Horn and C. R. Johnson, *Matrix Analysis* (Cambridge University Press, 1990).
[25] L. S. G. Kovásznay, J. Aeronautic. Sci. **20**, 657 (1953).
[26] S. J. Ali et al., Phys. Plasmas **25**, 092708 (2018).
[27] C. Huete Ruiz de Lira et al., Phys. Rev. E **83**, 056320 (2011).
[28] B. M. Haines et al., Phys. Plasmas **26**, 012707 (2019).